AGU PUBLICATIONS

JGR

Journal of Geophysical Research: Oceans

RESEARCH ARTICLE

10.1002/2016JC011875

Impact of model resolution for on-shelf heat transport along the West Antarctic Peninsula

Jennifer A Graham[1,2], Michael S Dinniman[1], and John M Klinck[1]

[1]Center for Coastal Physical Oceanography, Old Dominion University, Norfolk, Virginia, USA, [2]Now at Met Office Hadley Centre, Fitzroy Road, Exeter, UK

Key Points:
- Increased horizontal resolution allows for increased on-shelf heat transport and improved representation of on-shelf heat content
- Dominant cause of increased on-shelf heat transport differs between locations along the shelf-break
- Variability in on-shelf heat fluxes is dominated by changes in wind stress and shelf-break transport

Correspondence to:
J. A. Graham,
jennifer.graham@metoffice.gov.uk

Citation:
Graham, J. A, M. S Dinniman, and J. M. Klinck (2016), Impact of model resolution for on-shelf heat transport along the West Antarctic Peninsula, *J. Geophys. Res. Oceans*, *121*, 7880–7897, doi:10.1002/2016JC011875.

Received 11 APR 2016
Accepted 29 SEP 2016
Accepted article online 4 OCT 2016
Published online 28 OCT 2016

Abstract The flux of warm deep water onto Antarctic continental shelves plays a vital role in determining water mass properties adjacent to the continent. A regional model, with two different grid resolutions, has been used to simulate ocean processes along the West Antarctic Peninsula. At both 4 km and 1.5 km resolution, the model reproduces the locations of warm intrusions, as shown through comparison with observations from instrumented seals. However, the 1.5 km simulation shows greater on-shelf heat transport, leading to improved representation of heat content on the shelf. This increased heat transport is associated with increased eddy activity, both at the shelf-break and in the deep ocean off-shore. Cross-shelf troughs are key locations of on-shelf heat transport. Comparison of two troughs, Belgica and Marguerite, shows differing responses to increased resolution. At higher resolution, there is an increased on-shelf volume transport at Belgica Trough, but not at Marguerite Trough. This is likely related to the differing structure of the shelf-break jet between these two locations. The increased heat flux at Marguerite Trough is attributed to increased heat content in the on-shelf transport. Increased eddy activity off-shelf may lead to greater cross-front heat transport, and therefore increased heat available above the continental slope. While these simulations differ in their magnitude of heat transport, both show similar patterns of variability. Variations in wind stress lead to variations in speed of the shelf-break jet, and therefore on-shelf heat transport. These results demonstrate the importance of model resolution for understanding cross-shelf transport around Antarctica.

1. Introduction

The West Antarctic Peninsula (WAP) is one of the fastest warming regions on Earth [e.g., *Turner et al*., 2005; *Meredith and King*, 2005]. There has been a significant increase in ocean temperature both on and off the continental shelf [*Schmidtko et al*., 2014], and a significant decline in sea ice cover since the late 1970s [e.g., *Stammerjohn et al*., 2012; *Parkinson and Cavalieri*, 2012]. Circumpolar Deep Water (CDW) is the most voluminous water mass in the Southern Ocean, with temperature $>1.5^{\circ}$C, and salinity >34.7 [*Orsi et al*., 1995]. The core of CDW, characterized by a temperature maximum at depth, shoals toward the southern boundary of the Antarctic Circumpolar Current (ACC), reaching depths <300 m. *Schmidtko et al*. [2014] have shown that the CDW core has both warmed and shoaled since the 1970s. In regions where pure CDW has access to the continental shelf, such as the Amundsen-Bellingshausen Sea, they also show that this change in the deep ocean has coincided with warmer temperatures observed on the shelf. Increased shelf water temperatures have been cited as the dominant cause of increased mass loss from ice shelves along the West Antarctic coast [e.g., *Pritchard et al*., 2012; *Rignot et al*., 2013; *Wouters et al*., 2015; *Cook et al*., 2016]. Understanding the mechanisms of on-shelf heat transport is crucial for understanding variations in shelf water properties, and hence predicting future changes in the Antarctic mass budget, and global sea level rise.

Along the WAP, the southern boundary of the ACC, usually defined as the poleward limit of Upper Circumpolar Deep Water [*Orsi et al*., 1995], is adjacent to the continental shelf-break (Figure 1). This allows access of pure CDW to the continental shelf. Observations have shown that CDW crosses the shelf-break in particular locations, determined by bathymetry. In particular, warm deep water is found in deep, cross-shelf troughs [e.g., *Jenkins and Jacobs*, 2008; *Martinson and McKee*, 2012; *Zhang et al*., 2016; and Figure 2a]. *Klinck and Dinniman* [2010] outline a number of possible mechanisms for on-shelf transfer. For Marguerite Trough (Figure 1), the dominant mechanisms are believed to be flow-topography interactions and eddies shed from the along-shore flow. The internal Rossby radius

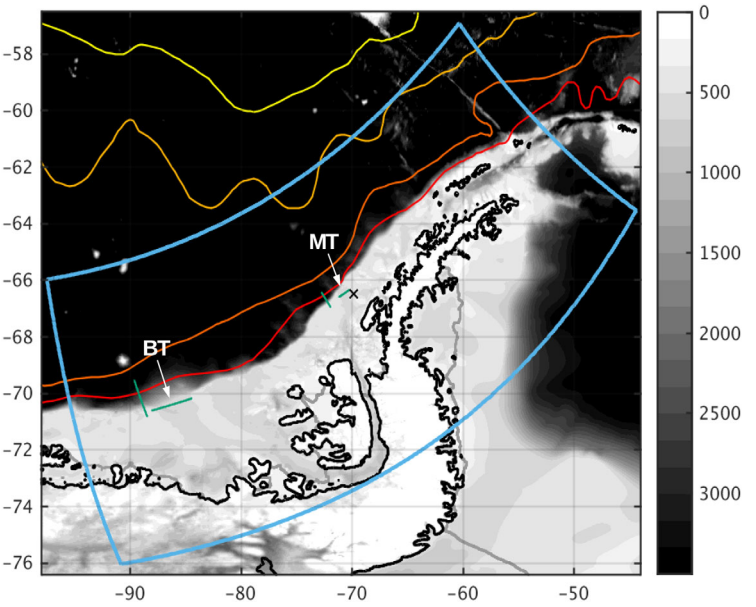

Figure 1. Map illustrating the location of the model domain (shown by the blue box) around the West Antarctic Peninsula. Gray shading shows bathymetry from Bedmap2 (m). Location of two cross-shelf troughs are indicated: Marguerite Trough (MT) and Belgica Trough (BT). Green lines show the position of "upstream" and "cross-trough" transects used for calculations or plots later in this paper. Black cross shows the location of a model mooring location, for comparison with observations at M1 in *Martinson and McKee* [2012]. Red-yellow lines show the observed position of ACC fronts [*Orsi et al.*, 1995].

on the WAP shelf is approximately 5 km, and observations have shown the presence of even smaller-scale features. Warm eddies have been observed in Marguerite Trough with a radius of 3−5 km [*Martinson and McKee*, 2012; *Moffat et al.*, 2009]. Using an idealized model of Marguerite Trough, *St-Laurent et al.* [2013] investigated the ability of numerical models to resolve such small-scale processes. Eddies that transported heat into the trough were only resolved with a grid spacing of <2 km. The heat transport associated with these eddies was shown to be comparable with that associated with the mean flow into the trough. Other studies have also shown the importance of model resolution and eddy processes, for on-shelf transfer around the continent. *Stewart and Thompson* [2015] have shown the importance of eddy processes for on-shelf CDW transfer across the Antarctic Slope Front, again recommending resolution <2 km. *Nakayama et al.* [2014] suggested that in order to correctly represent shelf properties in the Amundsen Sea, a resolution <5 km was required to resolve necessary flow-topography interactions. A number of regional studies are now beginning to use resolutions of 1.5 km to investigate variability on the Antarctic continental shelf [e.g., *Hattermann et al.*, 2014; *St-Laurent et al.*, 2015]. These studies all highlight the need for both accurate bathymetry and adequate resolution, in order to simulate ocean circulation around Antarctica.

This study presents two regional simulations of the WAP domain. Both simulations have the same atmospheric forcing and ocean boundary conditions, but have different horizontal resolution. Previous regional studies of the WAP [e.g., *Dinniman et al.*, 2011; *Nakayama et al.*, 2014] have typically used a resolution of $\sim$4 km. This resolution is here compared with a second simulation of 1.5 km resolution. Both simulations have been run for a period of 7 years. Through comparison of these two regional models, we can analyze the impact of increased resolution for simulating on-shelf heat transport and its effect on mean shelf water temperatures and variability. The results highlight the need for model improvements, as well as increased observations to monitor changes in this region.

2. Methods

2.1. Model Structure

The model used in this study is based on the Regional Ocean Modeling System (ROMS v3.6), which is widely used to study the Antarctic shelf seas [e.g., *Dinniman et al.*, 2007; *Galton-Fenzi et al.*, 2012; *Hattermann et al.*, 2014; *St-Laurent et al.*, 2015]. ROMS is a primitive equation, finite difference model, with a free surface and terrain-following vertical coordinates [*Haidvogel et al.*, 2008; *Shchepetkin and McWilliams*, 2009]. The version used here is coupled with a dynamic sea ice model [*Budgell*, 2005], which includes sea ice dynamics and thermodynamics [*Hunke and Dukowicz*, 1997; *Mellor and Kantha*, 1989; *Häkkinen and Mellor*, 1992]. A simple frazil ice model is also included [*Steele et al.*, 1989]. Thermodynamic and mechanical effects of static ice shelves are included, with the heat and salt transfer coefficients as functions of the friction velocity

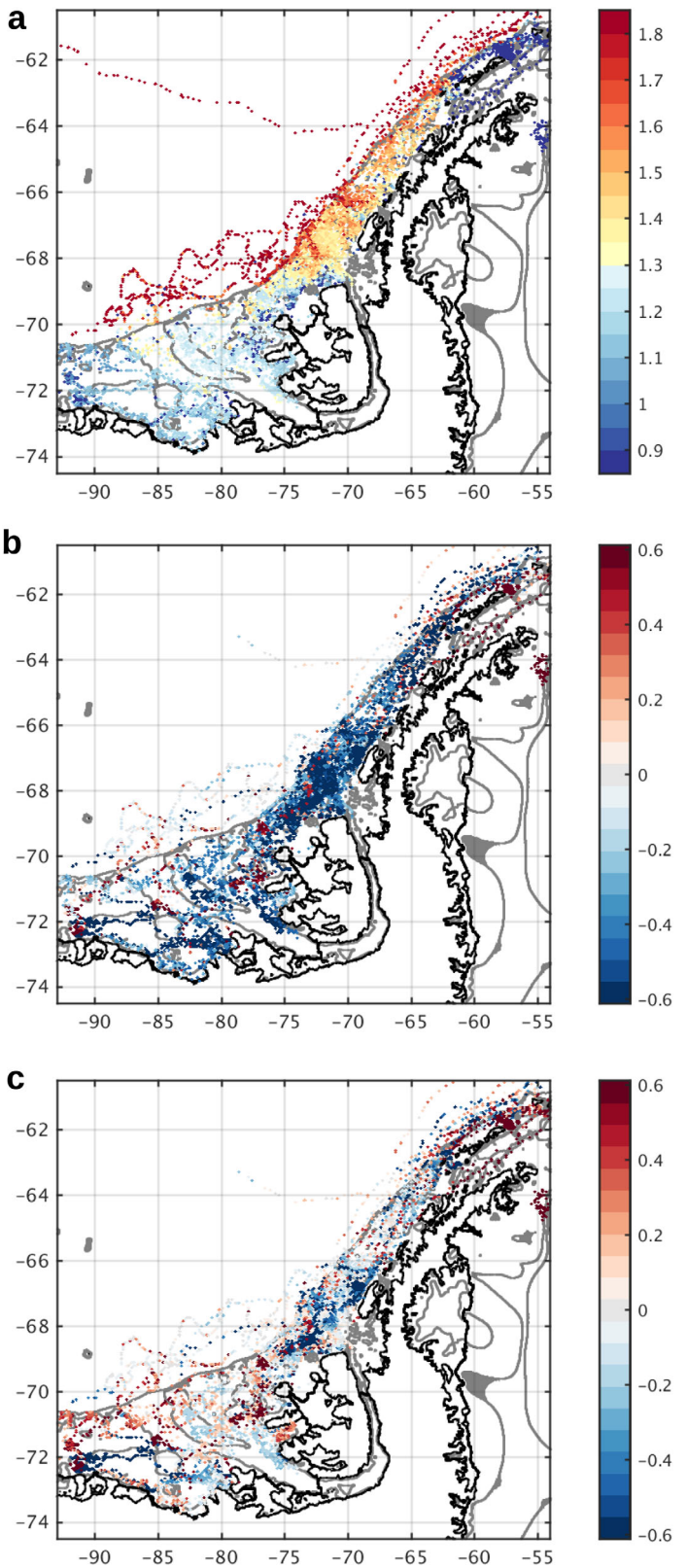

Figure 2. (a) Observations from tagged seals during 2009, maximum temperature below 200 m (°C). (b and c) Maximum temperature anomalies, comparing the mean model conditions for 2009 minus seal observations (shown in Figure 2a). (b) 4 km simulation minus seals, (c) 1.5 km simulation minus seals. For the anomalies, blue indicates the model biased cold, whereas red indicates the model is biased warm. Black contours show the coastline and extent of ice shelves; gray contours show the 500 and 1000 m isobaths, from Bedmap2.

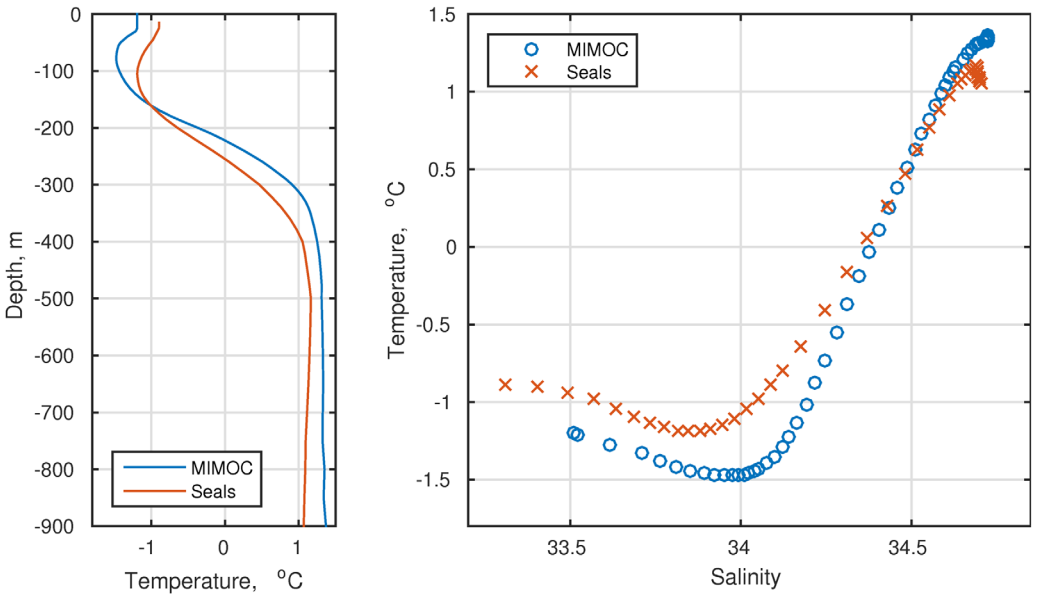

Figure 3. Mean temperature and salinity profiles, from MIMOC (blue) and tagged seal observations (red), for the southern Bellingshausen Sea shelf (95–75°W). (left) The mean temperature profile with depth. (right) The corresponding mean temperature-salinity profile. Note that profiles show the conditions averaged for January–March. MIMOC shows a climatology, whereas seal profiles are only from 2009. Therefore, there is expected to be some difference in the surface layer, reflecting potential differences in surface forcing. The maximum temperature below 200 m for the profiles shown is 1.37°C for MIMOC and 1.16°C for the seals.

[*Dinniman et al*., 2007; *Holland and Jenkins*, 1999]. Additional details regarding the model configuration can be found in *Dinniman et al*. [2011].

The domain used in this study was chosen for comparison with previous studies in the region [*Dinniman et al*., 2012], and extends from Thurston Island in the southwest, into the Scotia Sea, straddling the Antarctic Peninsula (Figure 1). Two grids are used, with grid spacing of approximately 4 km and 1.5 km, respectively, throughout the domain. Note that the same horizontal mixing parameters are used for both simulations, with a harmonic diffusivity coefficient of 5 $m^2\,s^{-1}$, and a harmonic viscosity coefficient of 0.1 $m^2\,s^{-1}$. Both have 24 vertical levels, with increased resolution at both the surface and base of the water column. A minimum water column thickness of 20 m is set throughout the domain. The model bathymetry and ice shelf draft have been interpolated from Bedmap2 south of 60°S [*Fretwell et al*., 2013], and GEBCO 2008 for bathymetry north of 60°S. Compared with earlier bathymetric products (including those used in *Dinniman et al*. [2012]), the greatest difference is seen in the southern portion of the domain, where there is improved representation of Belgica Trough [*Graham et al*., 2011]. Portions of the Wilkins Ice Shelf collapsed in 2008 and 2009, but Bedmap2 uses the precollapse extent. Since the simulations carried out here begin in 2006, the Bedmap2 extent has not been altered. Both the bedrock and ice shelves have been smoothed to reduce any pressure gradient errors that may arise from the terrain-following coordinates, and Abbot Ice Shelf has been masked at the western boundary.

2.2. Forcing and Initial Conditions

Open boundaries were treated following the methods outlined in *Dinniman and Klinck* [2004] and *Dinniman et al*. [2012]. Temperature and salinity on the lateral boundaries are nudged to a monthly mean climatology, provided from a combination of MIMOC [*Schmidtko et al*., 2013] and World Ocean Atlas 2013 (WOA13) [*Locarnini et al*., 2013; *Zweng et al*., 2013], obtained at 0.5° and 1° resolution, respectively. MIMOC is a monthly isopycnal/mixed-layer ocean climatology, available for the upper 1950 m. This product was chosen to provide a more accurate representation of seasonal mixed layer depth variability, preserving water mass properties. As MIMOC is only available in the upper 1950 m, WOA13 was used beneath this depth, with negligible difference found between the two products at the interface. Additional observations were available from seal profiles on the WAP continental shelf (Figure 2a). Tagged seal profiles were available for 2006–2010, with the highest number of profiles obtained during 2009 [*Padman et al*., 2012]. From these profiles, a mean temperature and salinity depth profile was calculated for the southern Bellingshausen shelf (Figure 3). Seals are tagged during

Austral summer and migrate north with the advance of sea ice, so the mean profile for the southern shelf was calculated for the period January–March 2009. Figure 3 shows that MIMOC has a higher maximum temperature on the southern Bellingshausen shelf than those observed by the seals (1.37°C and 1.16°C, respectively). At the western boundary of the domain, the mean seal profile is then used to represent the temperature and salinity beneath the mixed layer on the shelf. Here the temperature and salinity from the seal profile is then interpolated with depth beneath the 0°C isotherm. Velocity and sea surface height were obtained from the Simple Ocean Data Assimilation (SODA v2.2.4) ocean reanalysis [*Carton and Giese*, 2008], calculating a monthly mean climatology for each of the variables. Tidal forcing is not included. Monthly sea ice concentration is obtained from the Advanced Microwave Scanning Radiometer (AMSR-E, available up to October 2011) and Special Sensor Microwave Imager/Sounder (SSMIS, after October 2011). Both data sets were obtained at 6.25 km resolution [*Spreen et al.*, 2008]. While all ocean variables are applied with annually-repeating climatology at the lateral boundaries, sea ice concentration is applied with interannual variability.

Atmospheric forcing is provided from the Antarctic Mesoscale Prediction System (AMPS) archived forecasts [*Powers et al.*, 2012]. Data are obtained from March 2006 to December 2012, spanning two versions of the Polar Weather Research and Forecasting model (Polar WRF), with 20 and 15 km resolution, respectively. Cloud fraction is obtained from ERA-Interim [*Dee et al.*, 2011], since it is not available from the AMPS database. ERA-Interim was also used for all fields during January–February 2006, before the introduction of Polar WRF for AMPS. All necessary variables are applied as monthly means, except for wind vectors, which are provided at 6 hourly intervals. Open water surface heat and freshwater fluxes are calculated within ROMS using the COARE 3.0 bulk flux algorithm [*Fairall et al.*, 2003]. The higher resolution of AMPS, compared with available reanalysis products (e.g., ERA-Interim, with T255 spectral resolution, ~80 km), allows for improved representation of spatial variability around the Peninsula's steep topography [*Bromwich et al.*, 2013]. Resolving changes in both the speed and direction of winds along the coast, which play a key role in determining sea ice drift, polynya formation, and surface heat fluxes, can be critical to accurate simulation of Antarctic coastal waters [e.g., *Mathiot et al.*, 2012; *Hollands et al.*, 2013; *Dinniman et al.*, 2015].

Initial ocean conditions were taken from MIMOC and WOA13, as used for the forcing climatology, and the mean depth profile from the tagged seal observations (for conditions along the WAP shelf). As the mean seal profile is representative of late summer conditions (January–March), the model spin-up was then initialized in March 2006. Initial ice concentration is taken from AMSR-E, using the monthly mean from March 2006. Initial sea ice thickness is set as 0.5 m, with a snow thickness of 0.3 m.

2.3. Simulations

From initialization in March 2006, the 4 km model was run until December 2012, allowing adjustment to the chosen forcing and boundary conditions throughout the model domain. Following this spin-up simulation, the final conditions from December 2012 were used to initialize the model for a second simulation, January 2006 to December 2012. The 1.5 km model was initialized with conditions from the second 4 km simulation. Starting from March 2006, the 1.5 km model is run until December 2012, allowing adjustment to the increased grid resolution. The final conditions from this spin-up run were then used to initialize the 1.5 km model for a second January 2006 to December 2012 simulation. The results discussed here will refer to the January 2006 to December 2012 simulations for both resolutions (so both have a spin-up simulation, followed by a second for the results). With results from both models spanning 7 years, this allows for comparison of the mean shelf conditions, as well as potential interannual variability. The 4 km simulation was extended for a further two cycles, confirming that the level of drift following the initial spin-up run was negligible (not shown). During this extended run, each successive cycle showed similar patterns of interannual variability, and the overall drift in mean maximum temperature on the shelf was approximately −0.002°C per year. Therefore, we can assume that both the 4 km and 1.5 km are equilibrated for the simulations presented here, with model drift being a negligible contribution to any difference seen between them.

3. Results and Discussion

3.1. On-Shelf Heat Transport Comparison

Along the WAP, CDW is characterized by a temperature maximum beneath the mixed layer. Conditions vary through the simulation, but the maximum temperature beneath 200 m in mid-2009 (Figure 4) illustrates where CDW is typically transferred across the shelf-break (200 m is chosen as approximate depth of the

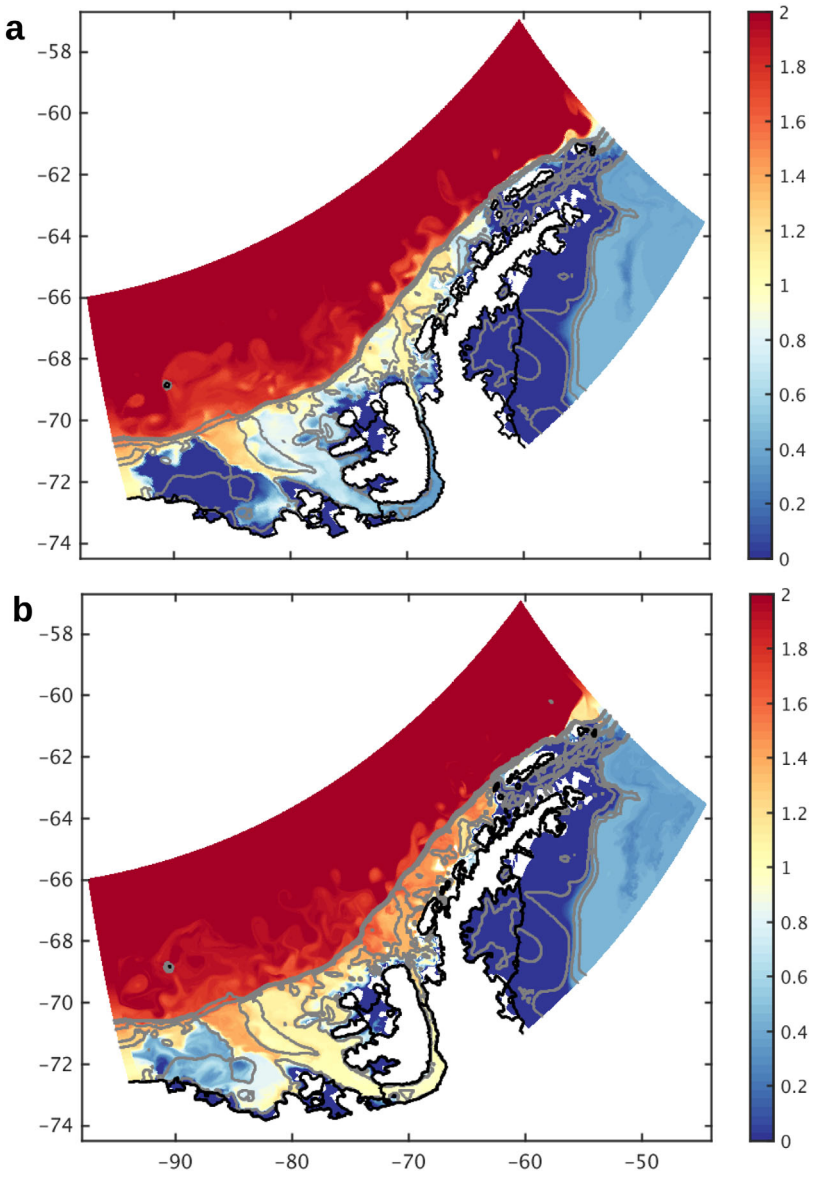

Figure 4. Maximum temperature below 200 m (°C), (a) 4 km simulation, (b) 1.5 km simulation. Both model simulations show 5 day-mean output, centered on 5 June 2009. Black contours show the coastline and extent of ice shelves; gray contours show the 500 and 1000 m isobaths, from model configuration.

pycnocline e.g., Figure 3a). Comparing these results with the seal observations from 2009 (Figure 2a), both models are able to reproduce the locations of warm intrusions on the shelf. Increased temperatures are found within cross-shelf troughs, such as Marguerite Trough (MT) in the north and Belgica Trough (BT) in the south. The quality of spatial variability in the models is aided by the quality of bathymetry used. Transport on the shelf tends to follow contours of planetary vorticity, f/H (where f is the Coriolis parameter and H is the ocean depth). On-shelf transfer is influenced by the shelf-break bathymetry, and away from the deep troughs, intrusions are also associated with smaller-scale bathymetric features. For example, warm intrusions can be found at approximately 67°S, in both simulations as well as the observations, associated with a shallower trough south of MT.

To assess the on-shelf transport of CDW, a passive tracer was released in all off-shelf waters with temperature >0°C, below 200 m. The tracer concentration has an initial value of one in all CDW off-shelf, and zero initial concentration on the shelf, where the on/off-shelf boundary is defined here as the 1000 m isobath along the continental slope. Figure 5 shows the evolution of tracer distribution during the first 3 months of

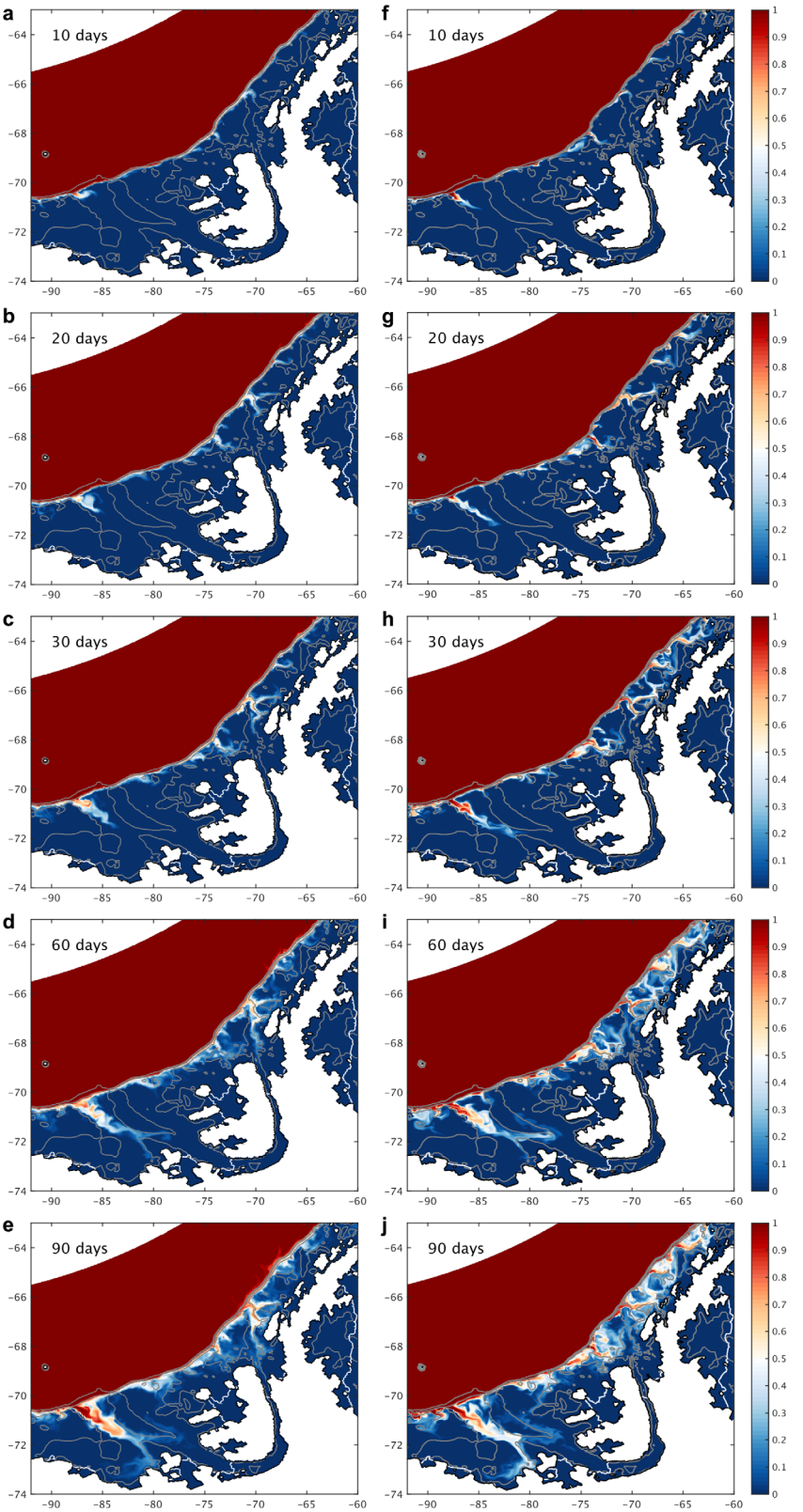

Figure 5. Maximum dye concentration [0-1] within the water column, (a–e) 4 km simulation and (f–j) 1.5 km simulation. Times shown are relative to the start of the simulation i.e., time since 1 January 2006. Each plot shows instantaneous output on that day. Black contours show the coastline; white contours show extent of ice shelves; gray contours show the 500 and 1000 m isobaths, from the model configuration.

the simulation. Intrusions of dye are visible on the shelf, illustrating that there are preferred locations of on-shelf transfer, typically associated with the shelf-break bathymetry. Within 10 days, increased concentrations are visible within the mouths of both MT and BT (Figures 5a and 5f). Intrusions are also visible away from these deeper troughs e.g., north of Wilkins Ice Shelf, and along the northern Peninsula. While the troughs are not the only locations of cross-shelf transfer, they play a key role in channeling the warm deep water toward the coast. This is particularly visible in BT, where the tracer extends from the shelf-break to the southern coast within the first 90 days (Figures 5e and 5j). A portion of the tracer that enters MT also branches northward (Figures 5b and 5g), contributing to the increased concentration visible on the northern shelf. The quality of the bathymetry used makes even the 4 km model a significant improvement on that used in previous studies, due to the presence of BT across the southern shelf. A similar tracer release study presented in *Dinniman et al*. [2011] shows virtually no tracer extending toward the southern coast after 60 days (their Figure 3). The distribution of the CDW tracer shown here is consistent with the temperature distribution seen on the shelf (Figure 4).

Although the location of intrusions is reproduced in both simulations, Figures 2 and 4 show that the subsurface maximum temperature in these intrusions is higher for the 1.5 km model. Observations show that the maximum temperature can exceed 1.4°C in BT and 1.8°C in MT (Figure 2a). For the 4 km model, the maximum temperature in BT exceeds 1.3°C, but is much lower than observed in MT, rarely exceeding 1.4°C (Figures 2b and 4a). The 1.5 km model shows temperatures exceeding 1.4°C in BT and 1.6°C in MT, closer to those observed (Figures 2c and 4b). It is worth noting that in Figures 2b and 2c, the instantaneous seal profiles are compared with mean model conditions for 2009. Therefore, a considerable amount of variability can be expected in the anomalies, due to temporal and spatial variability on the shelf. However, the difference between these two simulations remains clear. For the 4 km and 1.5 km models, the mean errors shown in Figures 2b and 2c are -0.40 ± 0.93°C and 0.03 ± 0.86°C, respectively. The mean maximum temperature over the whole WAP shelf varies during the simulation (Figure 6a), but has a time mean of 0.62°C for the 1.5 km model, compared with 0.14°C for the 4 km model. For comparison with the mean seal profile in Figure 3 (which shows a mean maximum temperature of 1.16°C), the mean maximum temperature over the southern shelf (west of 75°W) during January–March 2009 is 0.89°C for the 1.5 km model, compared with 0.40°C for the 4 km model. So the higher resolution model is able to provide a temperature distribution closer to observations across the shelf. Along with this, the time-mean heat content on the shelf increases from 1.62×10^{21} J for the 4 km model, to 1.95×10^{21} J for the 1.5 km model.

Here we focus on two cross-shelf troughs, MT and BT, where warm intrusions have been shown to occur in both the models and observations (Figures 2 and 4). MT has been a focus for previous observational campaigns, due primarily to its proximity to Antarctic research bases. BT is less accessible, with fewer observations, and therefore less is known about the circulation at this location. To capture the potential influence of eddies on heat fluxes, we need a sufficient frequency of temperature and velocity output. Observations from moorings in MT have shown that eddies typically have a radius of <5 km and drift with a background velocity of ~0.1 m s^{-1} [*Martinson and McKee*, 2012]. For the 7 year simulations, output is obtained at 5 day frequency (to focus on longer-term variability, and minimize computational resources required). However, eddies of this observed scale and speed would pass through a 1.5 km grid cell in one day, becoming less visible in 5 day-mean diagnostics. To assess the eddy heat fluxes, we then also ran a shorter simulation with 12 hourly output, for approximately 1 year (around 2008). This frequency is sufficient to capture the core of eddies within a 1.5 km grid spacing.

Figure 7 shows the mean heat transport across the shelf-break for the two simulations during 2008. The ocean heat transport, *OHT*, is calculated as

$$OHT = c_p\,\rho_0 \int_A v(\theta-\theta_f)\,dA$$

where v is the velocity perpendicular to the section (positive on-shore), θ_f is the freezing temperature (a lower limit of $\theta_f = -1.95$ is used here), A is the cross sectional area of the section, ρ_0 is the potential density, and $c_p = 3985$ J kg^{-1} K^{-1} is the specific heat. The heat transport here has been summed over 12 km bins, with the location of each bin shown by markers in the lower plot. This figure shows that both MT and BT are locations of peak heat transport, and these peaks are increased at higher resolution. The locations of maximum heat transport are consistent with the pathways of tracer shown in Figure 5, with inflows

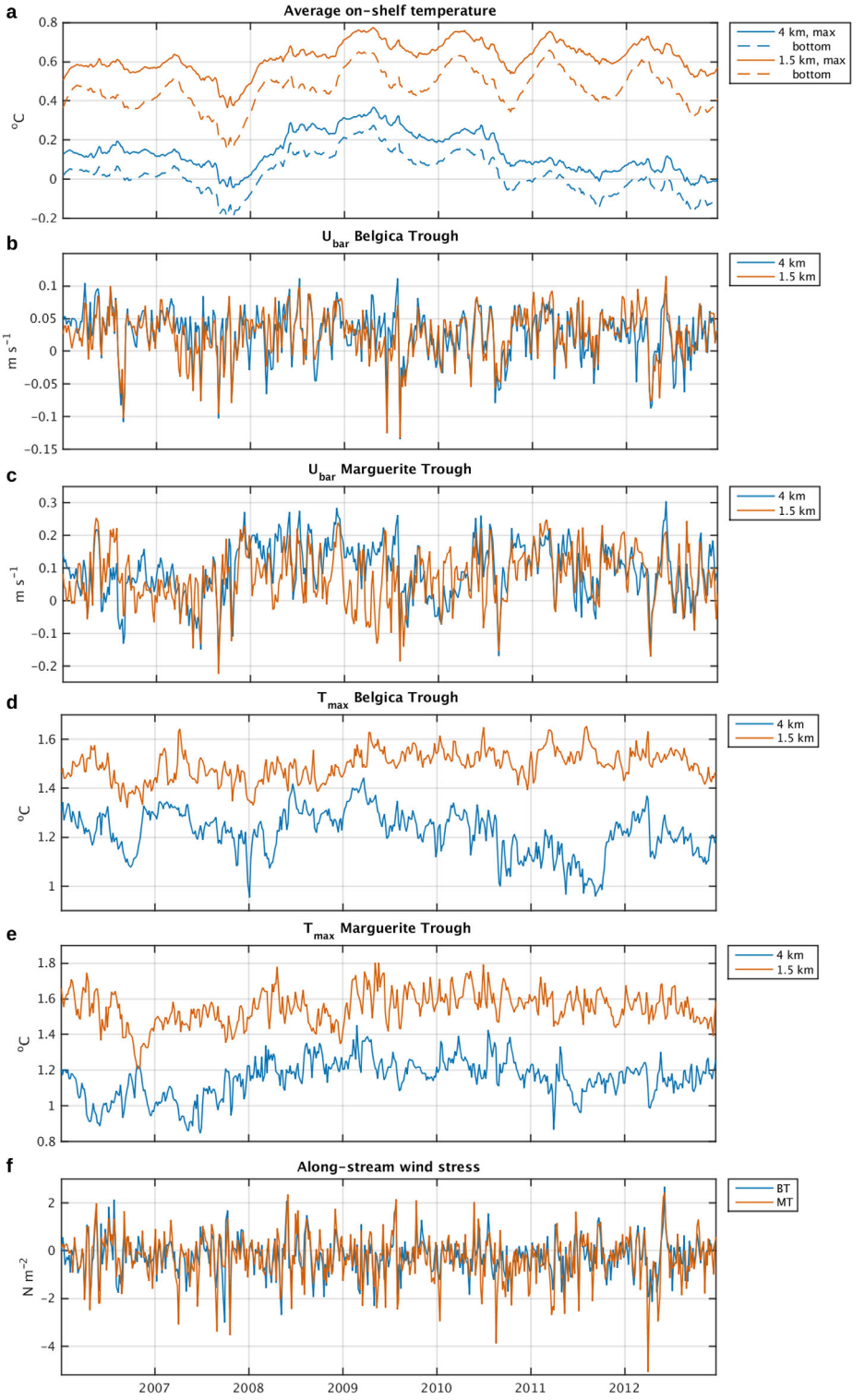

Figure 6. Time series of (a) mean maximum or bottom temperature on the WAP shelf; (b) vertical-mean along-shelf velocity, upstream of BT; (c) vertical-mean along-shelf velocity, upstream of MT; (d) maximum temperature in the shelf-break jet, upstream of BT; (e) maximum temperature in the shelf-break jet, upstream of MT; (f) wind stress component in the along-stream direction (note that here we neglect any potential impact of sea ice concentration on the drag coefficient). All values shown are 5 day-means. For Figures 6a–6e, blue and red lines refer to 4 km and 1.5 km resolution, respectively. For Figure 6f, blue and red refer to BT and MT, respectively. For Figures 6b–6f, the same locations are used for each MT or BT time series, using the location of the mean maximum velocity (illustrated in Figure 9). The along-stream direction follows the shelf-break, positive in the north-eastward direction.

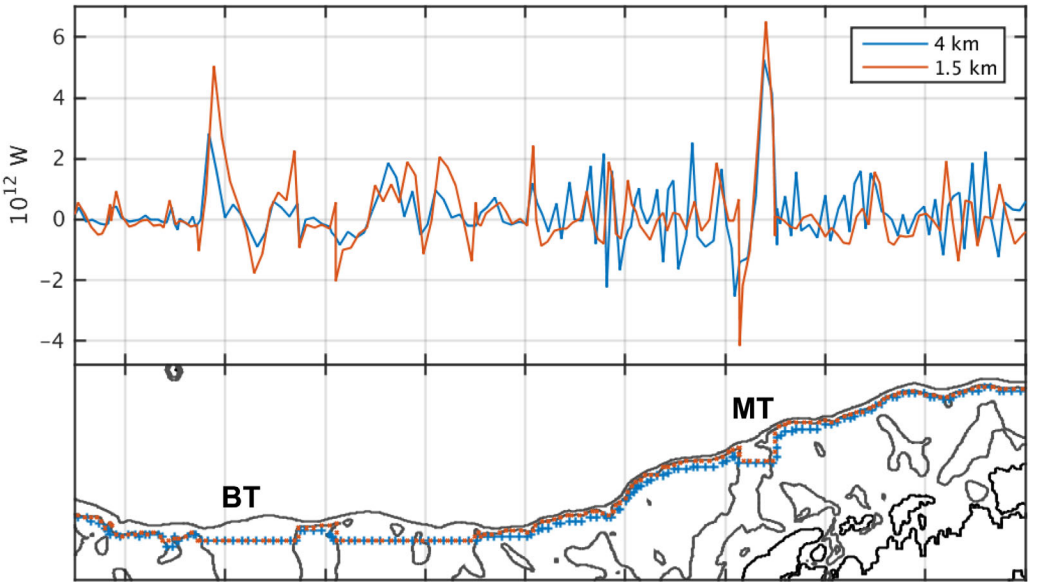

Figure 7. (top) Mean heat transport (10^{12} W) in relation to distance along the shelf-break. Heat transport has been summed over 12 km bins for both the 4 km (blue) and 1.5 km (red) simulations, and is positive in the on-shore direction. (bottom) Blue and red markers show the position of each bin along the shelf, for the respective lines above. Gray contours show the 500 and 1000 m isobaths. Black contours show the coastline. For MT and BT, the sections across the mouths of each trough match those shown in Figure 1.

predominantly entering the northern side of MT and western side of BT. Figures 8a and 8b then show the heat transport per unit area across the mouth of these two troughs (sections shown in Figure 1). As these sections do not have a zero net volume transport across them (while the net volume flux onto the whole continental shelf must be zero), it is important to bear in mind that the calculated heat transports do not provide an assessment of thermodynamic changes across the region. However, these sections can be used to provide a comparison of the heat transport between these two locations and resolutions. For the period shown in Figure 8, the mean heat transport at MT increased from $23.3 \pm 20.8 \times 10^4$ W m^{-2} at 4 km, to $28.4 \pm 25.2 \times 10^4$ W m^{-2} at 1.5 km (22% increase). The mean heat transport at BT also increased from 7.47 ± 8.07 to $10.8 \pm 9.4 \times 10^4$ W m^{-2} (46% increase). For both troughs, there is a large amount of variability, but there is a significant increase in heat transport at higher resolution.

A larger heat transport crossing the shelf-break may occur due to a larger volume transport of CDW, a higher temperature in the on-shelf flow, or a combination of these two. To assess the relative influence of the on-shelf volume transport, we can analyze the on-shelf transport of the passive tracer. The tracer has the same initial value in all CDW off-shelf, so the on-shelf tracer transport gives an indication of the CDW transport into the trough, irrespective of its total heat content. Figures 8c and 8d show the transport of this tracer across the mouths of MT and BT for the same period as the heat transport time series. For both troughs, there is again a large amount of variability, with similar patterns to those seen for the heat transport. However, when looking at the overall difference between the two resolutions, there is a significant increase in the mean dye transport for BT, but not for MT. For the period shown, the mean transport of dye into BT increased from 0.39 ± 0.41 to 0.55 ± 0.49 dye units Sv (41% increase), whereas the transport into MT had a smaller increase, from 0.42 ± 0.37 to 0.43 ± 0.37 dye units Sv (2% increase). Therefore, while there is a comparable increase in both volume and heat transport into BT, the 22% increase in heat transport at MT cannot be explained by the CDW volume alone.

Figure 9 shows the mean temperature and along-shore current, upstream of BT and MT for the duration of the simulation (2006–2012). For both locations, there is an increased temperature within the along-shore current at higher resolution. The mean maximum temperature within the along-shore jet increases from 1.15 to 1.55°C at MT, and from 1.22 to 1.50°C at BT (Figures 6d and 6e). This mean is calculated across 10 and 20 km sections, for MT and BT, respectively (the narrower width due to the steeper slope at MT), centered on the location of the mean maximum current above the slope. Therefore, there is a greater heat

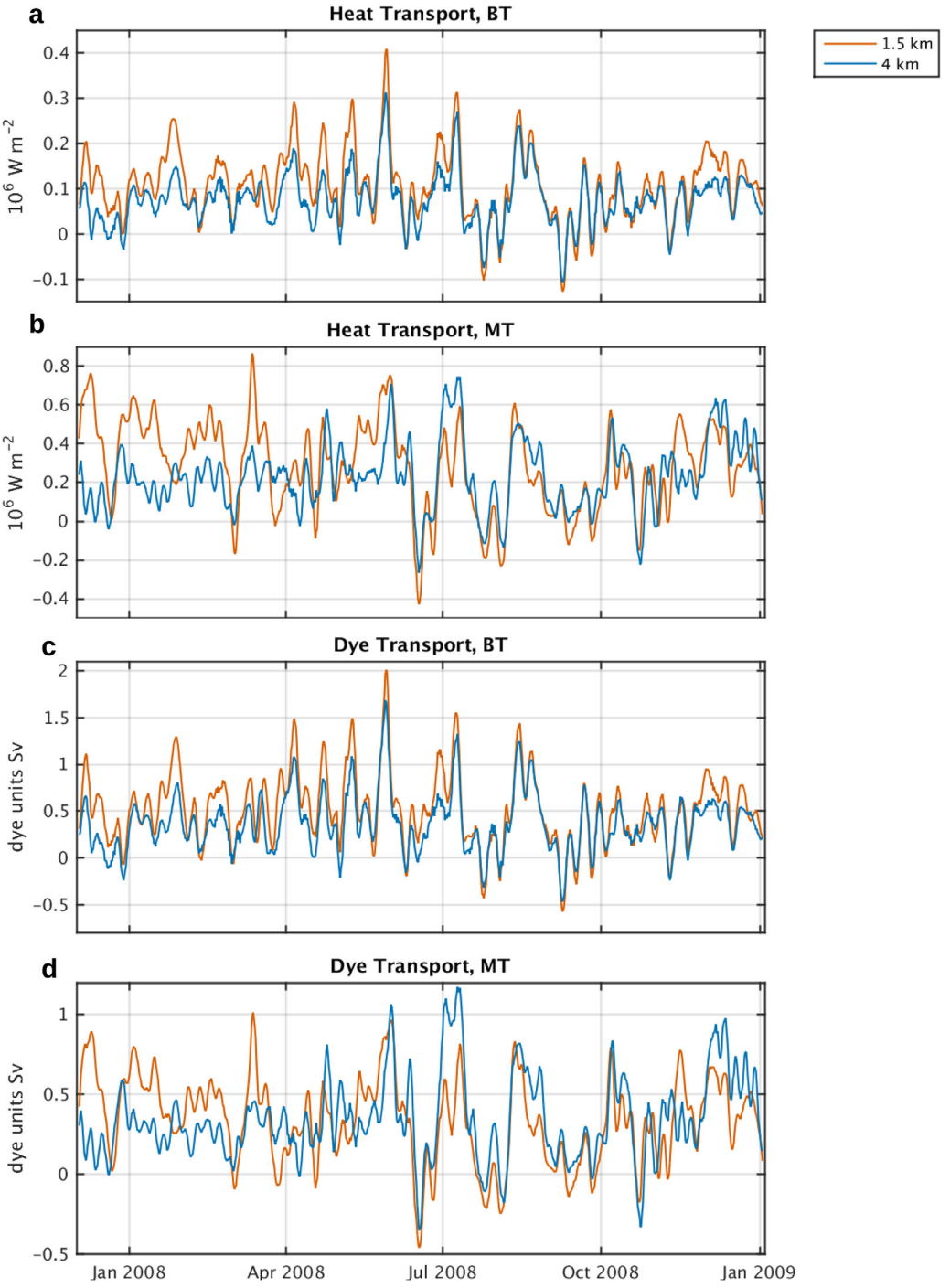

Figure 8. Time series of (a and b) heat transport (10^6 W m^{-2}), (c and d) dye transport (dye units Sv). Transports are calculated across the mouth of the troughs (Figure 1) from 12 hourly output, and are positive in the on-shelf direction. Values shown have been smoothed using a 3 day running mean.

content available for on-shelf transport. Both simulations have the same boundary conditions and atmospheric forcing, therefore the difference in heat distribution must occur due to changes in circulation or mixing within the model domain. This could result from either a southward shift in the position of ACC fronts, or greater eddy heat flux across these fronts. There is some difference in the mean structure of the shelf-break jet, with increased baroclinicity at higher resolution. This is likely associated with the increased deep water temperature present above the slope, leading to increased stratification. However, there is no

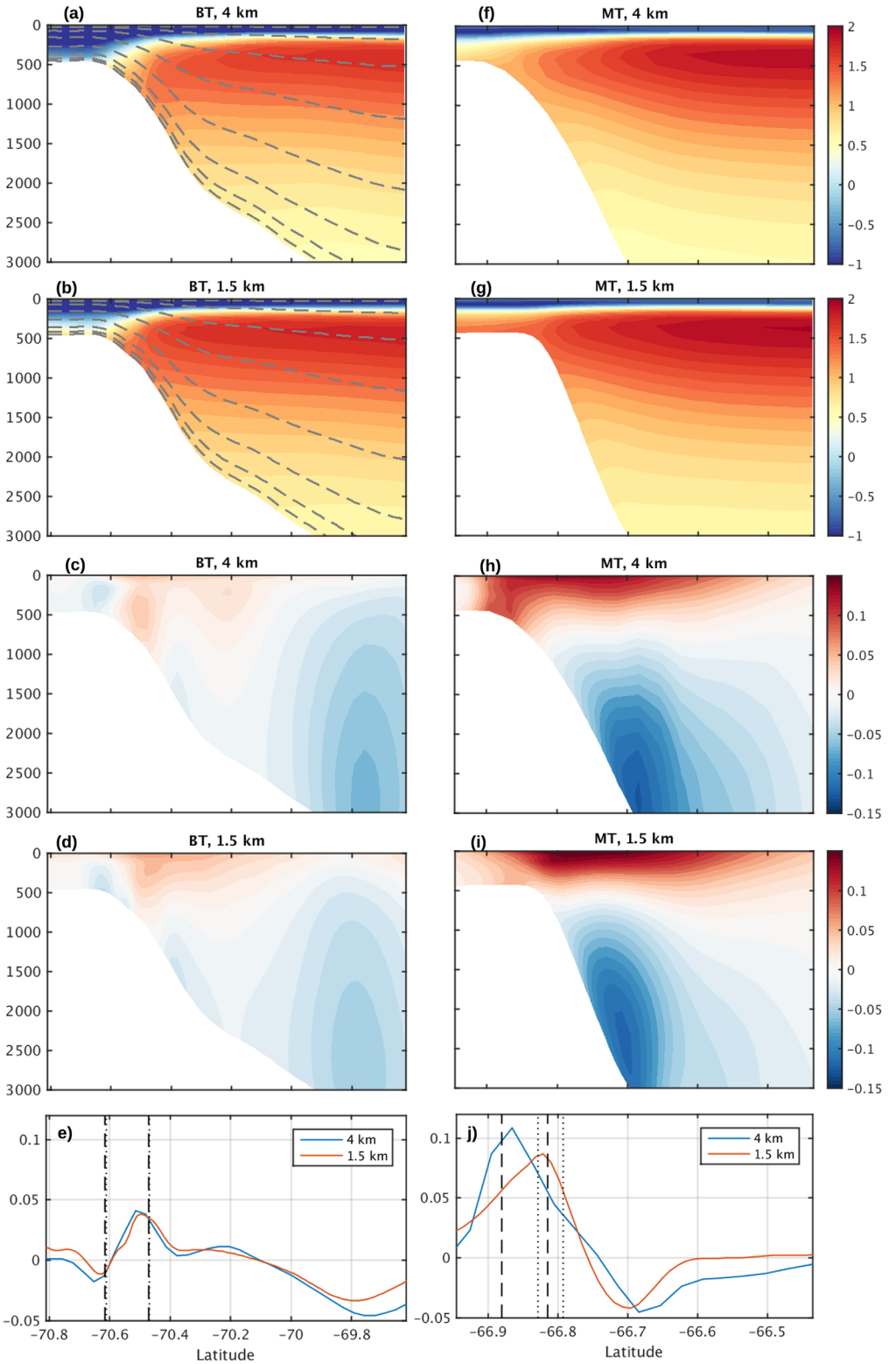

Figure 9. Cross sections of (a, b, f, and g) temperature (°C) and (c–e and h–j) velocity ($m\,s^{-1}$), upstream of Marguerite or Belgica troughs (MT or BT). Gray contours in Figures 9a and 9b show the position of the terrain-following depth coordinates (S-levels), showing every third level for clarity. Figures 9e and 9j show the depth-averaged velocity across each section, with blue and red lines showing the conditions for the 4 km and 1.5 km simulations. Black vertical lines show the location of the 500 and 1000 m isobaths, with dashed and dotted lines showing those for the 4 km and 1.5 km simulations, respectively. For velocity, positive is in the north-eastward direction, following the shelf-break. All figures show the mean conditions for the 2006–2012 simulation.

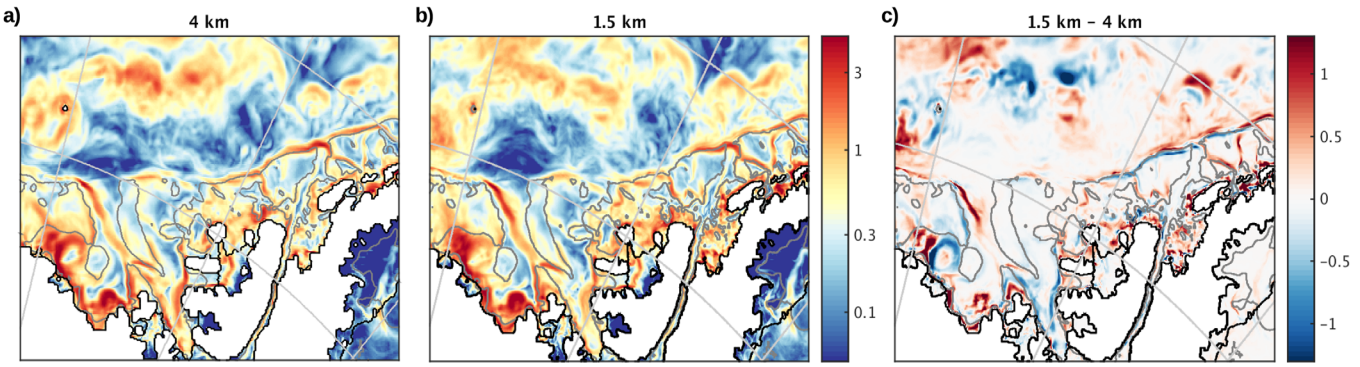

Figure 10. Mean eddy kinetic energy (EKE), calculated from depth-mean velocity (10^{-3} m^2 s^{-2}) for (a) 4 km, (b) 1.5 km, and (c) anomaly (1.5 km − 4 km). Mean EKE is calculated over 2008 (for the period shown in Figure 8). Note the use of logarithmic scale on the color axis for Figures 10a and 10b. Gray contours show the model 500 m isobaths.

significant difference in the mean position of the depth-averaged current (Figures 9e and 9j). We define the position of the jet above the slope as the associated isobath, rather than a geographical position. For both the 4 km and 1.5 km simulations, the peak current remains above approximately 550 m upstream of MT and 800 m upstream of BT (Figures 9e and 9j). At both locations, there is also no increase in the mean depth-average current when moving to higher resolution (Figures 6b, 6c, 9e and 9j). For BT, the mean along-shore current is 4.1 and 3.8 cm s^{-1}, for 4 km and 1.5 km, respectively. At MT, the mean along-shore current sees a decrease from 10.9 to 8.7 cm s^{-1}, with increased resolution (evident in Figure 6c during 2008–2009). However, there is an increase in mean eddy activity at higher resolution, both on and off the continental shelf (Figure 10). Net heat transport across Southern Ocean fronts results from the balance between northward Ekman transport and southward eddy heat fluxes [e.g., *Dufour et al.*, 2015; *Naveira Garabato et al.*, 2011]. Increased eddy activity off-shelf is then a potential contributor to the increased heat content above the slope.

Although both troughs experience an increased heat transport with higher resolution, the mechanisms responsible are different. BT has a significant increase in volume transport (Figure 8), whereas MT is predominantly influenced by an increased heat content adjacent to the shelf-break. This difference is likely a result of the differing structure of along-shore transport found at the shelf-break. Upstream of BT, the along-shore flow is centered above the slope, between the 500 and 1000 m isobath (Figures 9c–9e). At MT, the along-shore flow peaks closer to 500 m, and extends onto the shelf-break (Figures 9h–9j). There is also increased baroclinicity above the slope at MT than there is at BT. A stronger baroclinic component is consistent with the steeper slope around MT. There is a lack of full-depth velocity observations along the WAP slope for comparison. However, *Pennel et al.* [2012] have shown that the stability of a coastal current is dependent on the ratio of the bathymetric slope to the isopycnal slope. With steeper bathymetry, at MT we can then expect a stable current with increased baroclinicity above the slope. *St-Laurent et al.* [2013] show that the mechanisms of on-shelf heat transport are influenced by the structure of the shelf-break jet, relative to the bathymetry. For the case of a wide shelf-break jet extending onto the shelf, on-shelf heat transport is dominated by interactions of the mean-flow and topography, which may be resolved at lower resolution (3 km). However, for the case of a narrow jet positioned over the slope, Rossby waves interact with the topography and make a significant contribution to the heat flux, which can only be resolved at higher resolution ($<$2 km). Comparing the jet structure in these idealized simulations [*St-Laurent et al.*, 2013, Figure 2] with the two troughs here (Figures 9e and 9j), the profile seen at MT is similar to that of the wide shelf-break jet, extending onto the shelf, whereas BT has a jet removed from the shelf-break, above the slope. We then propose that the different structures of the along-shore flow may then explain the differing response in on-shore transport at these two locations. At higher resolution, BT could see a greater impact from resolving wave-topography interactions (and eddy-fluxes), contributing to a significant increase in volume flux into the trough. However, the transport into MT is likely dominated by mean-flow interactions with topography, where the inertia in the along-shore current encourages flow into the cross-shelf troughs [*Dinniman et al.*, 2011].

Figure 11 shows the heat transport anomalies into each trough. From the *OHT* definition above, we define temperature, $T = \theta - \theta_f$, and calculate relative contributions in each simulation from

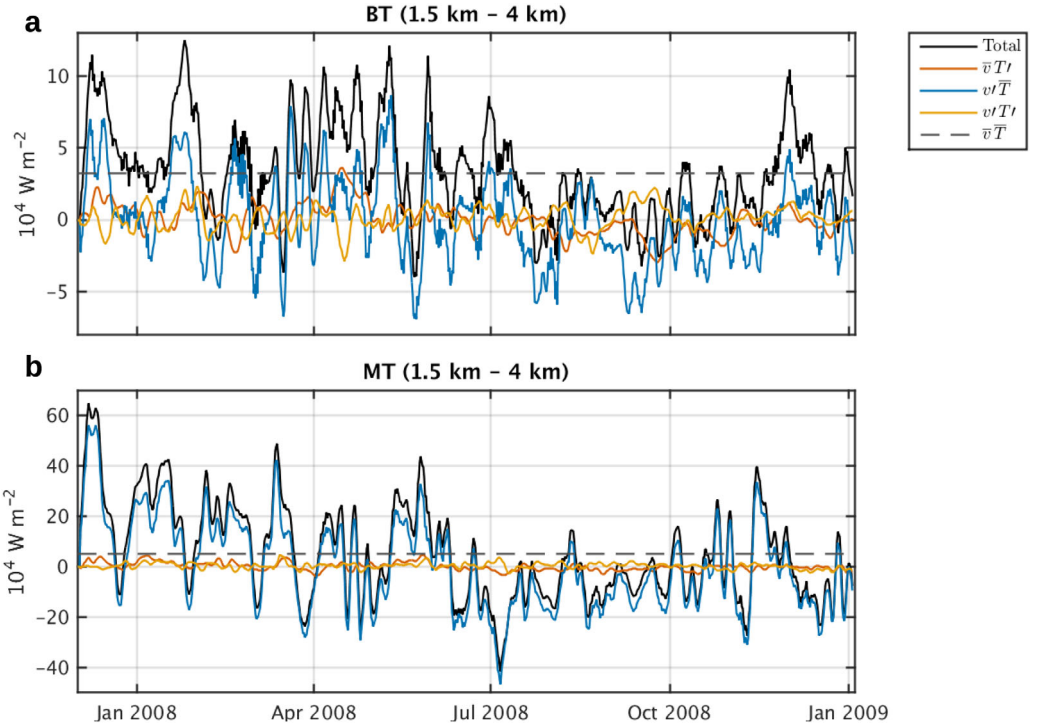

Figure 11. Time series of heat transport anomalies (10^4 W m^{-2}), across the mouths of (a) BT and (b) MT. For each simulation, the total heat transport (black) has been decomposed into contributions from $\bar{v}\,\bar{T}$ (dashed), $\bar{v}\,T'$ (red), $v'\,\bar{T}$ (blue), and $v'\,T'$ (yellow), as defined in the text. Anomalies for each component are shown, as 1.5 km−4 km. Values shown have been smoothed using a 3 day running mean.

$$v\,T = \bar{v}\,\bar{T} + \bar{v}\,T' + v'\,\bar{T} + v'\,T'$$

where overbar denotes the mean for the duration of the 2008 simulation. This demonstrates the role of mean temperature and flow versus eddy heat flux contributions. Along with the total anomaly, Figure 11 then also shows the anomalies for each component of the heat transport (1.5 km–4 km for each). For both troughs, the contribution from $\bar{v}\,\bar{T}$ is close to the mean difference in heat transport between these two simulations. However, in terms of the variability, we see the largest contribution from velocity perturbations. At MT, the other components appear negligible for the total heat transport anomaly. At BT, velocity perturbations also show the largest contribution to variability, however the contributions from temperature perturbations, and $v'\,T'$, are closer in magnitude at this location. This supports the suggestion that eddy fluxes may have a greater impact at BT. Figure 10c shows an increased EKE around both troughs at higher resolution, but with a greater increase at the mouth of BT. Eddy-fluxes do still play a key role at MT (compensating for the decreased upstream current); however mean changes in heat content must play a more significant role to account for the increased heat transport at this location (remember that the CDW dye transport into MT was essentially unchanged with increased resolution). The variability in heat transport will be discussed further in the following section.

It is worth noting here that eddy fluxes also play a key role in transporting heat on-shore from the shelf-break (Figure 10). Figure 12 shows temperature as a function of depth and time from a model mooring on the northern side of MT (location shown in Figure 1). This location was chosen to match that presented in *Martinson and McKee* [2012] (see their Figure 4). From the two simulations presented here, the 1.5 km model is able to reproduce the middepth warm cores that have been observed in MT. The 4 km simulation shows a reduced heat content on the shelf, but also a different vertical profile, with the maximum temperature typically found at the base of the water column rather than mid-depth. Therefore, the 1.5 km model is able to reproduce the nature of heat transport onto the shelf, as well as the magnitude.

3.2. Heat Transport Variability

While the heat transport onto the shelf increases at high resolution, the patterns of variability remain similar (Figures 8 and 12). As both models receive annually-repeating ocean forcing at the lateral boundaries,

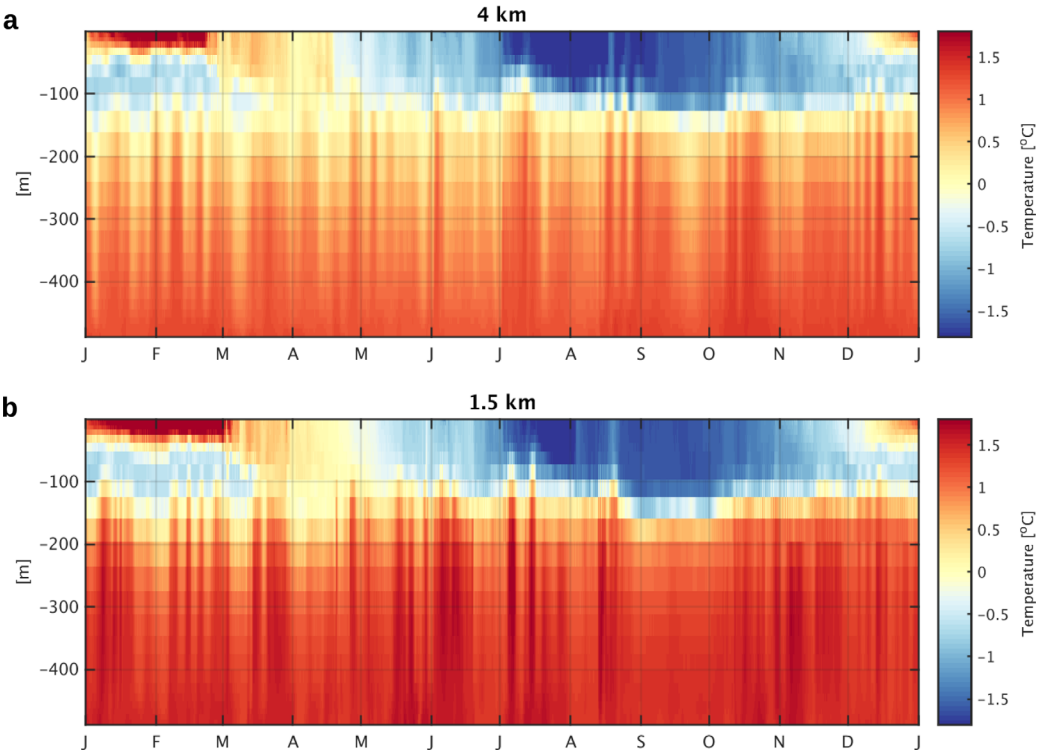

Figure 12. Temperature as a function of depth and time at a model mooring location on the northern side of MT (Figure 1), for 2008 during the two simulations: (a) 4 km and (b) 1.5 km.

interannual variability must result from the differences in surface forcing. *Dinniman et al.* [2011] showed that upstream of MT, the flux into the trough varied with changes in the along-shore wind stress, with a peak correlation between the wind stress and heat flux at a lead time of 2 days. This resulted from the wind stress influencing the speed of the shelf-break jet. Aside from the influence of eddy fluxes, onshore flow is strongly determined by the inertia in the shelf-break jet (i.e., the speed of the upstream current). For the simulations here, Figure 11 has shown that the variability of heat transport into both Marguerite and Belgica troughs is strongly dependent on the velocity variability at these locations. Here we find a peak correlation between the wind stress and heat transport with a lead time of 24–36 h (for 1.5 km (4 km), significant correlations of 0.32 (0.43) and 0.33 (0.42), for MT and BT; significance defined here as a correlation with $p < 0.01$). This can be attributed to a significant correlation between the along-shore wind stress and upstream current with a lead time of 12 h (correlations of 0.26 (0.46) and 0.34 (0.36), for 1.5 km (4 km) at MT and BT), as well as significant correlations between the upstream current and heat transport into the trough with a lead of 12 h (0.43 (0.53) and 0.50 (0.42), for 1.5 km (4 km) at MT and BT).

Throughout the simulation, there is evidence of changes in both the along-shore current and along-shore wind stress (Figures 6b 6c, and 6f). There is a considerable range of variability on shorter timescales (i.e., submonthly), but also patterns of long-term, interannual variability. For example, both models show decreased current velocities in early 2007, moving to increased velocity in 2008. This increase in the along-shelf flow correlates with an increase in on-shelf deep water temperature seen between 2007 and 2008 (Figure 6a). During 2007, there is an increased occurrence of negative wind stress over the shelf-break (i.e., southwestward wind stress). This would lead to a on-shore Ekman transport, and decreased SSH gradient across the shelf-break. In 2008, there is then an increased occurrence of positive wind stress (northeastward), which would contribute to an increased SSH gradient over the shelf-break. Note that this variability corresponds to an increased observed heat content in 2008 versus 2007 at a mooring on the northern side of MT [*Martinson and McKee*, 2012, Figures 4 and 5].

Aside from the variations in current speed, we also see variations in temperature adjacent to the shelf-break (Figures 6d and 6e). The proximity of the CDW core to the shelf-break may be influenced by meandering

jets, or upwelling/downwelling isopycnals. As with the wind stress, there is also a significant correlation between the wind stress curl and the heat transport into the troughs. In theory, upwelling winds at the shelf-break could allow for a shoaling of CDW, and therefore increased heat transport. However, during this simulation the heat transport onto the shelf shows a greater dependency on the speed of the shelf-break jet. The correlation between the maximum temperature in the along-shore current and heat transport into the troughs is only significant for the 4 km simulation at MT, with correlations for 4 km (1.5 km) of 0.24 (−0.07) and −0.02 (−0.09), for MT and BT. While the temperature was a strong factor in increased heat transport between the two simulations, the current speed plays a more dominant role within each simulation.

Previous studies have identified shoaling CDW as a mechanism for long-term warming trends in the Amundsen-Bellingshausen Sea [*Schmidtko et al*., 2014]. These simulations show that the flow speed along the shelf-break has a greater impact on short term variability. Unfortunately we have few observations of the currents in this region to assess whether this has also played a role in the recently published trends [*Schmidtko et al*., 2014]. The available heat does have a clear impact, as evidenced by the increased heat transport at higher resolution, associated with increased temperature at the shelf-break. It is possible that heat content may play a more significant role over decadal time scales. However, longer high-resolution simulations would be required to investigate the relative influence of these processes.

4. Conclusions

The two simulations presented here show that while a 4 km grid spacing is able to reproduce the locations of warm intrusions on the shelf, the magnitude of on-shelf heat transport increases at 1.5 km resolution. Cross-shelf transfer locations are influenced by bathymetry. Therefore, the use of updated bathymetry makes the 4 km model a significant improvement on earlier models of this region. However, further observations are needed to reduce the error in these bathymetric products, particularly in the southern Bellingshausen Sea, which has fewer observations, and yet has a strong influence on cross-shelf transport through BT.

To compare these two models, this study has focussed on two cross-shelf troughs (MT and BT), which both see increased transport at high resolution, but via differing dominant mechanisms. The differing response to higher resolution may be a result of the shelf-break jet, which has different structures at the two locations. The two structures have been compared with the idealized studies presented by *St-Laurent et al*. [2013]. BT has a narrower jet positioned over the slope, so that eddies and wave-topography interactions may make a more significant contribution at higher resolution. At BT, there is a significant increase in both volume transport and heat content at higher resolution. MT has a wider shelf-break jet, so the on-shelf heat transport is dominated by the mean flow, which can be resolved at lower resolution. The shoreward volume transport of CDW at MT does not see a significant increase at higher resolution, but there is a greater heat content available for on-shelf advection. There is an increase in mean EKE both on and off the shelf, but we see a larger increase within BT than in MT. This supports the suggestion that eddies make a larger contribution to the increased transport at this location.

While there is a difference in the magnitude of heat transport, there are strong similarities in the variability within these two models. Variability in on-shelf heat transport can be influenced by both temperature and velocity at the shelf-break. These processes are both influenced by atmospheric forcing. For the time period of this study, the shelf-break current was found to have the dominant influence, with increased along-shelf flow speed leading to increased on-shelf heat transport. For both troughs, at both resolutions, the speed of the current was found to have a significant correlation with the along-stream (northeastward) wind stress. This is consistent with previous modelling studies of the region [*Dinniman et al*., 2011].

While this study has focussed on heat transport, CDW is also believed to be a source of nutrients for the Antarctic shelf ecosystem [e.g., *Prézelin et al*., 2000, 2004]. The difference in transport seen in the northern end of the Pensinsula is then particularly relevant for ongoing observations around the Palmer LTER (Long-Term Ecological Research). Eddies play a key role in transporting CDW on-shore from the shelf-break, and cannot be resolved at lower resolution. This highlights the need for regional biogeochemical models to have adequate resolution to resolve this influence.

This study emphasizes the importance of both model resolution and bathymetry for representing water mass variability on Antarctic continental shelves. Given the observed and predicted changes to water masses around the continent, it is important that future studies either use adequate resolution, or are aware of their limitations. Idealized studies suggest that a resolution <2 km is required [e.g., *St-Laurent et al*., 2013; *Stewart and Thompson*, 2015]; however, further tests in realistic configurations are needed to confirm the resolution needed for heat transport convergence. Resolving eddy processes is crucial for determining mechanisms of variability, influences on floating ice shelves, and therefore future Antarctic ice mass balance. While these models do include static ice shelves, a full investigation of basal melt rates and melt water transport will be the subject of future study, and has therefore not been discussed here. However, for ice shelves with deep grounding lines, whose melt rates depend on the deep shelf temperatures (e.g., George VI) [*Holland et al*., 2010], one can expect that the increased heat content at higher resolution will be associated with increased basal melt rates. If we want to fully understand changes to the Antarctic environment, we need eddy-resolving ocean models.

Acknowledgments

This research was supported by the Turing High Performance Computing cluster at Old Dominion University (ODU). The data for this study are stored on the ODU mass storage system, and are available upon request to the corresponding author (Jennifer Graham, jennifer.graham@metoffice.gov.uk). This work was partially supported by a grant from the National Science Foundation (ANT-0944223), and Public Weather Service (PWS) funding at the Met Office, UK. We would also like to thank two anonymous reviewers for their constructive comments, which significantly improved this manuscript.

References

Bromwich, D. H., F. O. Otieno, K. M. Hines, K. W. Manning, and E. Shilo (2013), Comprehensive evaluation of polar weather research and forecasting performance in the Antarctic, *J. Geophys. Res. Atmos.*, *118*, 274–292, doi:10.1029/2012JD018139.

Budgell, P. (2005), Numerical simulation of ice-ocean variability in the Barents Sea region, *Ocean Dyn.*, *55*, 370–387, doi:10.1007/s10236-005-0008-3.

Carton, J., and B. Giese (2008), A reanalysis of ocean climate using Simple Ocean Data Assimilation (SODA), *Mon. Weather Rev.*, *136*, 2999–3017.

Cook, A. J., P. R. Holland, M. P. Meredith, T. Murray, A. Luckman, and D. G. Vaughan (2016), Ocean forcing of glacier retreat in the western Antarctic Peninsula, *Science*, *353*, 283–286, doi:10.1126/science.aae0017.

Dee, D. P., et al. (2011), The ERA-Interim reanalysis: Configuration and performance of the data assimilation system, *Q. J. R. Meteorol. Soc.*, *137*, 553–597, doi:10.1002/qj.828.

Dinniman, M. S., and J. M. Klinck (2004), A model study of circulation and cross-shelf exchange on the west Antarctic Peninsula continental shelf, *Deep Sea Res., Part II*, *51*, 2003–2022, doi:10.1016/j.dsr2.2004.07.030.

Dinniman, M. S., J. M. Klinck, and W. O. Smith Jr. (2007), Influence of sea ice cover and icebergs on circulation and water mass formation in a numerical circulation model of the Ross Sea, Antarctica, *J. Geophys. Res.*, *112*, C11013, doi:10.1029/2006JC004036.

Dinniman, M. S., J. M. Klinck, and W. O. Smith Jr. (2011), A model study of Circumpolar Deep Water on the West Antarctic Peninsula and Ross Sea continental shelves, *Deep Sea Res., Part II*, *58*, 1508–1523, doi:10.1016/j.dsr2.2010.11.013.

Dinniman, M. S., J. M. Klinck, and E. E. Hofmann (2012), Sensitivity of Circumpolar Deep Water transport and ice shelf basal melt along the West Antarctic Peninsula to changes in the winds, *J. Clim.*, *25*, 4799–4816, doi:10.1175/JCLI-D-11-00307.1.

Dinniman, M. S., J. M. Klinck, L.-S. Bai, D. H. Bromwich, K. M. Hines, and D. M. Holland (2015), The effect of atmospheric forcing resolution on delivery of ocean heat to the Antarctic floating ice shelves, *J. Clim.*, *28*, 6067–6085, doi:10.1175/JCLI-D-14-00374.1.

Dufour, C. O., et al. (2015), Role of mesoscale eddies in cross-frontal transport of heat and biogeochemical tracers in the Southern Ocean, *J. Phys. Oceanogr.*, *45*, 3057–3081, doi:10.1175/JPO-D-14-0240.1.

Fairall, C., E. Bradley, J. Hare, A. Grachev, and J. Edson (2003), Bulk parameterization of air-sea fluxes: Updates and verification for the COARE algorithm, *J. Clim.*, *16*, 571–591, doi:10.1175/1520-0442(2003)016 $<$ 0571:BPOASF$>$2.0.CO;2.

Fretwell, P., et al. (2013), Bedmap2: Improved ice bed, surface and thickness datasets for Antarctica, *Cryosphere*, *7*, 375–393, doi:10.5194/tc-7-375-2013.

Galton-Fenzi, B. K., J. R. Hunter, R. Coleman, S. J. Marsland, and R. C. Warner (2012), Modeling the basal melting and marine ice accretion of the Amery Ice Shelf, *J. Geophys. Res.*, *117*, C09031, doi:10.1029/2012JC008214.

Graham, A. G. C., F. O. Nitsche, and R. D. Larter (2011), An improved bathymetry compilation for the Bellingshausen Sea, Antarctica, to inform ice-sheet and ocean models, *Cryosphere*, *5*, 95–106.

Haidvogel, D. B., et al. (2008), Ocean forecasting in terrain-following coordinates: Formulation and skill assessment of the Regional Ocean Modeling System, *J. Comput. Phys.*, *227*, 3595–3624, doi:10.1016/j.jcp.2007.06.016.

Häkkinen, S., and G. L. Mellor (1992), Modeling the seasonal variability of a coupled Arctic ice-ocean system, *J. Geophys. Res.*, *97*, 20,285–20,304, doi:10.1029/92JC02037.

Hattermann, T., L. H. Smedsrud, O. A. Nøst, J. M. Lilly, and B. K. Galton-Fenzi (2014), Eddy-resolving simulations of the Fimbul Ice Shelf cavity circulation: Basal melting and exchange with open ocean, *Ocean Modell.*, *82*, 28–44, doi:10.1016/j.ocemod.2014.07.004.

Holland, D. M., and A. Jenkins (1999), Modeling thermodynamic ice-ocean interactions at the base of an ice shelf, *J. Phys. Oceanogr.*, *29*, 1787–1800.

Holland, P. R., A. Jenkins, and D. M. Holland (2010), Ice and ocean processes in the Bellingshausen Sea, Antarctica, *J. Geophys. Res.*, *115*, C05020, doi:10.1029/2008JC005219.

Hollands, T., V. Haid, W. Dierking, R. Timmermann, and L. Ebner (2013), Sea ice motion and open water area at the Ronne Polynia, Antarctica: Synthetic aperture radar observations versus model results, *J. Geophys. Res. Oceans*, *4*, 1940–1954, doi:10.1002/jgrc.20158.

Hunke, E., and J. Dukowicz (1997), An elastic-viscous-plastic model for sea ice dynamics, *J. Phys. Oceanogr.*, *27*, 1849–1867, doi:10.1175/1520-0485(1997)027 $<$ 1849:AEVPMF$>$2.0.CO;2.

Jenkins, A., and S. Jacobs (2008), Circulation and melting beneath George VI Ice Shelf, Antarctica, *J. Geophys. Res.*, *113*, C04013, doi:10.1029/2007JC004449.

Klinck, J. M., and M. S. Dinniman (2010), Exchange across the shelf break at high southern latitudes, *Ocean Sci.*, *6*, 513–524, doi:10.5194/os-6-513-2010.

Locarnini, R. A., et al. (2013), World Ocean Atlas 2013, in *Volume 1: Temperature*, *NOAA Atlas NESDIS 73*, edited by S. Levitus and A. Mishonov, NOAA Atlas NESDIS, *73*, 40 pp.

Martinson, D. G., and D. C. McKee (2012), Transport of warm Upper Circumpolar Deep Water onto the western Antarctic Peninsula continental shelf, *Ocean Sci.*, *8*, 433–442, doi:10.5194/os-8-433-2012.

Mathiot, P., N. C. Jourdain, B. Barnier, H. Gallée, J. M. Molines, J. L. Sommer, and T. Penduff (2012), Sensitivity of coastal polynyas and high-salinity shelf water production in the Ross Sea, Antarctica, to the atmospheric forcing, *Ocean Dyn.*, *62*, 701–723, doi:10.1007/s10236-012-0531-y.

Mellor, G., and L. Kantha (1989), An ice-ocean coupled model, *J. Geophys. Res.*, *94*, 10,937–10,954, doi:10.1029/JC094iC08p10937.

Meredith, M. P., and J. C. King (2005), Rapid climate change in the ocean west of the Antarctic Peninsula during the second half of the 20th century, *Geophys. Res. Lett.*, *32*, L19604, doi:10.1029/2005GL024042.

Moffat, C., B. Owens, and R. C. Beardsley (2009), On the characteristics of Circumpolar Deep Water intrusions to the west Antarctic Peninsula continental shelf, *J. Geophys. Res.*, *114*, C05017, doi:10.1029/2008JC004955.

Nakayama, Y., R. Timmermann, M. Schröder, and H. Hellmer (2014), On the difficulty of modeling Circumpolar Deep Water intrusions onto the Amundsen Sea continental shelf, *Ocean Modell.*, *84*, 26–34.

Naveira Garabato, A. C., R. Ferrari, and K. L. Polzin (2011), Eddy stirring in the Southern Ocean, *J. Geophys. Res.*, *116*, C09019, doi:10.1029/2010JC006818.

Orsi, A. H., T. Whitworth III, and W. D. Nowlin Jr. (1995), On the meridional extent and fronts of the Antarctic Circumpolar Current, *Deep Sea Res., Part I*, *42*, 641–673.

Padman, L., et al. (2012), Oceanic controls on the mass balance of Wilkins Ice Shelf, Antarctica, *J. Geophys. Res.*, *117*, C01010, doi:10.1029/2011JC007301.

Parkinson, C. L., and D. J. Cavalieri (2012), Antarctic sea ice variability and trends, *Cryosphere*, *6*, 871–880, doi:10.5194/tc-6-871-2012.

Pennel, R., A. Stegner, and K. Béranger (2012), Shelf impact on buoyant coastal current instabilities, *J. Phys. Oceanogr.*, *42*, 39–61, doi:10.1175/JPO-D-11-016.1.

Powers, J., K. W. Manning, D. H. Bromwich, J. J. Cassano, and A. M. Cayette (2012), A decade of Antarctic science support through AMPS, *Bull. Am. Meteorol. Soc.*, *93*, 1699–1712, doi:10.1175/BAMS-D-11-00186.1.

Prézelin, B. B., E. E. Hofmann, C. Mengelt, and J. M. Klinck (2000), The linkage between Upper Circumpolar Deep Water (UCDW) and phytoplankton assemblages on the west Antarctic Peninsula continental shelf, *J. Mar. Res.*, *58*, 165–202, doi:10.1357/002224000321511133.

Prézelin, B., E. Hofmann, M. Moline, and J. Klinck (2004), Physical forcing of phytoplankton community structure and primary production in continental shelf waters of the Western Antarctic Peninsula, *J. Mar. Res.*, *62*, 419–460, doi:10.1357/0022240041446173.

Pritchard, H. D., S. R. M. Ligtenberg, H. A. Fricker, D. G. Vaughan, M. R. van den Broeke, and L. Padman (2012), Antarctic ice-sheet loss driven by basal melting of ice shelves, *Nature*, *484*, 502–505, doi:10.1038/nature10968.

Rignot, E., S. Jacobs, J. Mouginot, and B. Scheuchl (2013), Ice-shelf melting around Antarctica, *Science*, *341*, 266–270, doi:10.1126/science.1235798.

Schmidtko, S., G. C. Johnson, and J. M. Lyman (2013), MIMOC: A global monthly isopycnal upper-ocean climatology with mixed layers, *J. Geophys. Res. Oceans*, *118*, 1658–1672, doi:10.1002/jgrc.20122.

Schmidtko, S., K. J. Heywood, A. F. Thompson, and S. Aoki (2014), Multidecadal warming of Antarctic waters, *Science*, *346*, 1227–1231, doi:10.1126/science.1256117.

Shchepetkin, A. F., and J. C. McWilliams (2009), Correction and commentary for "Ocean forecasting in terrain-following coordinates: Formulation and skill assessment of the Regional Ocean Modeling System" by *Haidvogel et al.*, *J. Comput. Phys.*, *228*, 8985–9000, doi:10.1016/j.jcp.2009.09.002.

Spreen, G., L. Kaleschke, and G. Heygster (2008), Sea ice remote sensing using AMSR-E 89 GHz channels, *J. Geophys. Res.*, *113*, C02S03, doi:10.1029/2005JC003384.

St-Laurent, P., J. M. Klinck, and M. S. Dinniman (2013), On the role of coastal troughs in the circulation of warm Circumpolar Deep Water on Antarctic shelves, *J. Phys. Oceanogr.*, *43*, 51–64, doi:10.1175/JPO-D-11-0237.1.

St-Laurent, P., J. M. Klinck, and M. S. Dinniman (2015), Impact of local winter cooling on the melt of Pine Island Glacier, Antarctica, *J. Geophys. Res. Oceans*, *120*, 6718–6732, doi:10.1002/2015JC010709.

Stammerjohn, S., R. Massom, D. Rind, and D. Martinson (2012), Regions of rapid sea ice change: An interhemispheric seasonal comparison, *Geophys. Res. Lett.*, *39*, L05502, doi:10.1029/2012GL050874.

Steele, M., G. L. Mellor, and M. G. McPhee (1989), Role of the molecular sublayer in the melting or freezing of sea ice, *J. Phys. Oceanogr.*, *55*, 139–147, doi:10.1175/1520-0485(1989)019 < 0139:ROTMSI>2.0.CO;2.

Stewart, A. L., and A. F. Thompson (2015), Eddy-mediated transport of warm Circumpolar Deep Water across the Antarctic shelf break, *Geophys. Res. Lett.*, *42*, 432–440, doi:10.1002/2014GL062281.

Turner, J., S. R. Colwell, G. J. Marshall, T. A. Lachlan-Cope, A. M. Carleton, P. D. Jones, V. Lagun, P. A. Reid, and S. Iagovkina (2005), Antarctic climate change during the last 50 years, *Int. J. Climatol.*, *25*, 279–294, doi:10.1002/joc.1130.

Wouters, B., A. M.-E. nol, V. Helm, T. Flament, J. M. van Wessem, S. R. M. Ligtenberg, M. R. van den Broeke, and J. L. Bamber (2015), Dynamic thinning of glaciers on the Southern Antarctic Peninsula, *Science*, *348*, 899–903, doi:10.1126/science.aaa5727.

Zhang, X., A. F. Thompson, M. M. Flexas, F. Roquet, and H. Bornemann (2016), Circulation and meltwater distribution in the Bellingshausen sea: From shelf break to coast, *Geophys. Res. Lett.*, *43*, 6402–6409, doi:10.1002/2016GL068998.

Zweng, M., et al. (2013), World Ocean Atlas 2013, in Volume 2: Salinity, NOAA Atlas NESDIS 74, edited by S. Levitus and A. Mishonov, NOAA Atlas NESDIS *74*, 39 pp.